Shock Waves (2024) 34:497–513
https://doi.org/10.1007/s00193-024-01202-4

ORIGINAL ARTICLE

Normal shock wave coherence relative to other flow events with high and low levels of inlet Mach wave unsteadiness

W. Manneschmidt[1] · P. M. Ligrani[1] · M. Sorrell[1] · A. M. Ciccarelli[1] · B. Weigand[2]

Received: 25 January 2024 / Revised: 27 September 2024 / Accepted: 28 September 2024 / Published online: 27 November 2024

Abstract
Considered are interactive relationships between a normal shock wave and the downstream shock wave leg of the associated lambda foot, as well as between a normal shock wave and time-varying static pressure as measured along the bottom surface of the test section. Such relationships are investigated as they vary with two different magnitudes of inlet unsteady Mach wave intensity and are characterized using shadowgraph flow visualization data, as well as power spectral density, magnitude-squared coherence, and time lag data. Employed for the investigation is a specialty test section with an inlet Mach number of 1.54, as utilized within a transonic/supersonic wind tunnel. The resulting data provide evidence of distinct interactions over a wide range of frequencies between the normal shock wave and the downstream shock wave leg of the lambda foot for low inlet unsteady Mach wave intensity. Note that these are not present in the same form and over the same ranges of frequency with high inlet unsteady Mach wave intensity. These differences are partially due to the location where flow events originate. The most significant sources of flow unsteadiness within the present investigation are mostly associated with the normal and oblique shock waves (with low inlet unsteady Mach wave intensity), and mostly with inlet flow disturbances from unsteady Mach waves (with high inlet unsteady Mach wave intensity). The present experimental results additionally evidence important connections between the normal shock wave and unsteady flow events within lower portions of the lambda foot, especially near the adjacent boundary layer separation region.

Keywords Shock waves · Mach waves · Supersonic flow · Compressible flow · Unsteady flow · Turbulence · Experimental aerodynamics

List of symbols

Variables

C_{xy}	Magnitude-squared coherence of signals x and y
f	Frequency, Hz
GS	Gray scale intensity of an image pixel
HT	High inlet unsteady Mach wave intensity
i	Index number
LT	Low inlet unsteady Mach wave intensity
N	Number of frames
P	Instantaneous gray scale value of a pixel for a single visualization frame
P_i	Instantaneous gray scale value of a pixel for a single visualization frame
PSD	Gray scale power spectral energy
t	Time
x	Streamwise coordinate
y	Normal coordinate
z	Spanwise coordinate
τ_{xy}	Time lag of signals x and y

Superscripts

$\prime$	Fluctuation value
—	Time-averaged value

Communicated by E. Timofeev.

✉ P. M. Ligrani
pml0006@uah.edu

[1] Propulsion Research Center, Department of Mechanical and Aerospace Engineering, University of Alabama in Huntsville, Alabama 35899, USA

[2] Institute of Aerospace Thermodynamics (ITLR), University of Stuttgart, 70569 Stuttgart, Germany

1 Introduction

A number of investigations consider shock wave interaction unsteadiness, as well as associated instantaneous flow

structural characteristics. For example, Humble et al. [1] consider the three-dimensional instantaneous structure of shock wave/turbulent boundary layer interactions. A conceptual model of the boundary layer which approaches a shock wave, provided by these investigators, indicates that vortical structures are associated with relatively low-speed regions, whereas relatively high-speed regions "fill-in the separation between these structures." Ganapathisubramani and Clemens [2, 3] also investigate and describe significant coherence between the upstream boundary layer and downstream shock wave unsteadiness. Touber and Sandham [4] describe a different perspective, wherein low-frequency interaction region unsteadiness is not a result of forcing, either from the upstream or downstream boundary layer, but "an intrinsic property of the coupled system." In contrast, Piponniau et al. [5], Grilli et al. [6], Wu and Martin [7], and Pirozzoli et al. [8] consider shock wave interactions with the flow separation bubble beneath the shock wave structure to be more important and indicate that unsteadiness in the interaction region is related to pulsations of the separation region. An important result from the Pirozzoli et al. [8] investigation ties the strength of the oncoming shock wave, as well as the resulting interaction, to formation and development of the recirculation bubble. Additional perspectives on such phenomena are provided by Clemens and Narayanaswamy [9]. According to these investigators, interaction strength is directly related to the strength or relative size of separation, which is characterized by the magnitude of separated flow length scales. This strength also determines the degree to which an interaction exhibits sensitivity to upstream or downstream fluctuations. Clemens and Narayanaswamy [9] further indicate that both upstream and downstream mechanisms are present within all interactions, where the importance and effects of both mechanisms change as separation strength varies. Overall, the downstream mechanism dominates for strongly separated flows, and combined upstream and downstream mechanisms dominate for weakly separated flows. Here, strong and weakly separated flows are distinguished by local velocity magnitudes of recirculating flows, local turbulence intensity values within and near to flow reattachment regions, and the sizes of streamwise length scales which characterize flow recirculation zones.

Within the present study, considered are interactive relationships between a normal shock wave and the downstream shock wave leg of the associated lambda foot, as well as interactive relationships between a normal shock wave and time-varying static pressure as measured along the bottom surface of the test section. Such relationships are investigated as they vary with two different magnitudes of inlet unsteady Mach wave intensity, as quantified by high and low levels. A shadowgraph system is employed to visualize time-varying, shock wave flow features within a volume (as a line-of-sight integrated image), which covers most of the span of the test section. The resulting gray scale flow visualization time-sequence data are acquired and digitized, in parallel with the acquisition of time-varying surface static pressure data. Results from these measurements are then processed to determine frequency spectra, magnitude-squared coherence values, and associated time lag magnitudes.

Employed for the investigation is a specialty test section with an inlet Mach number of 1.54, as utilized within a transonic/supersonic wind tunnel system. Different inlet unsteady Mach wave intensity levels are associated with different numbers and different amounts of unsteadiness of families of intersecting and interacting Mach waves, which are located within and just downstream of the test section entrance. Low inlet unsteady Mach wave intensity is present with minimal Mach waves present. This arrangement is achieved using a polished interior nozzle surface, and no geometric discontinuities between the nozzle exit and the test section entrance. High inlet unsteady Mach wave intensity is achieved with abundant unsteady Mach waves present. To produce this flow condition, slight nozzle interior surface roughness is present (prior to nozzle surface polishing), along with installed surface discontinuities between the nozzle exit and the test section entrance. The resulting data provide evidence of distinct interactions over a wide range of frequencies between the normal shock wave and the downstream shock wave leg of the lambda foot. These interactions are observed to change significantly with inlet unsteady Mach wave intensity level, with differences that are partially a consequence of the location where unsteady flow events originate.

As such, results from the present investigation are different from previous studies because of consideration of unsteady interactions and coherence of flow phenomena associated with a normal shock wave relative to flow events at other locations. No other shock wave investigation is known which employs such an approach.

Presented within the sections which follow are discussions of experimental apparatus and procedures, data acquisition and analysis procedures, and experimental results. These sections are followed by a summary and conclusions.

2 Experimental apparatus and procedures

2.1 Wind tunnel and test section

A transonic/supersonic wind tunnel is used for the present study, which operates in a blow-down mode. Systems upstream of the nozzle include an air compressor, a series of air dryers and filters, five separate and inter-connected air storage/supply tanks (with a total volume of 40 m^3), a series of valves, a pneumatic flow control valve, a pressure-regulating gate valve, an air diverter plenum with a 12-m^3 volume, and inlet ducting. After passing through the nozzle

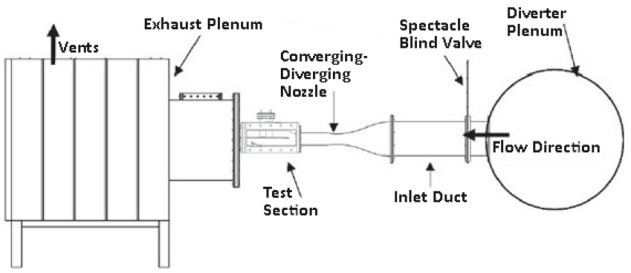

Fig. 1 Leg of transonic/supersonic wind tunnel employed for the present investigation

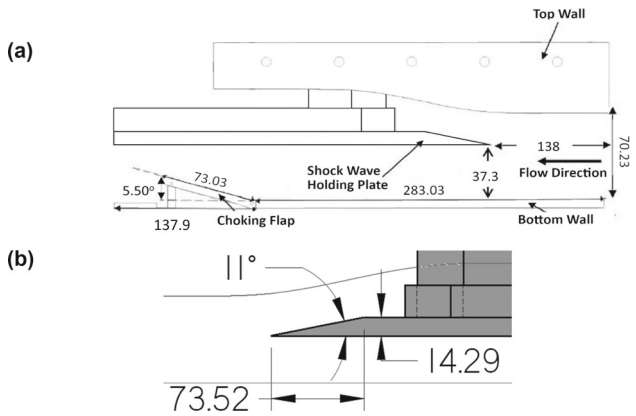

Fig. 2 **a** Test section employed for the present investigation. **b** Details of leading edge of shock wave holding plate. All dimensions are given in millimeters

and the test section, air enters the downstream plenum with a volume of 2 m^3. Air then flows out through several pipes and noise baffles to exhaust outside the building. Figure 1 presents a diagram of the facility which spans locations from the air-diverter plenum upstream of the test section to the exhaust plenum just downstream of the test section.

Figure 2a displays a detailed diagram of the test section, which is comprised of a flat bottom wall, a diverging top wall, and two side walls. Also included are the shock wave holding plate used to position and stabilize the normal shock wave, the top wall from which the shock wave holding plate is mounted, and the choking flap. Details of the leading edge of the shock wave holding plate are provided within Fig. 2b. For the present investigation, the streamwise position of the shock wave holding plate is 138.4 mm downstream of the nozzle exit, the bottom of the shock wave holding plate is 37.3 mm above the bottom wall, and the shock wave choking flap is positioned at an angle of 5.50 degrees. The test section inlet Mach number is 1.54, where Mach number is defined as the local flow velocity divided by the local flow sonic velocity. Additional information on the experimental

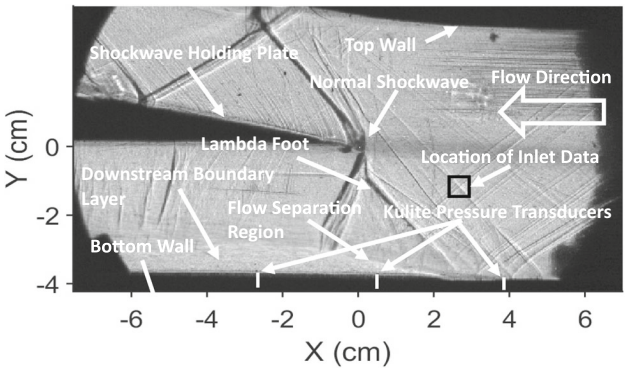

Fig. 3 Flow test section configuration, including Kulite pressure transducer locations (K1 is at $x = -2.69$ cm, K2 is at $x = 0.71$ cm, and K3 is at $x = 3.86$ cm), inlet locations to characterize and quantify inlet unsteady Mach wave intensity, and coordinate system

facility, including the test section, is provided by Ligrani and Marko [10].

2.2 Surface-mounted Kulite pressure transducers

Within the test section, mounted along the bottom wall at three different streamwise positions, are three XCQ-062 Kulite pressure transducers. The Kulite pressure transducers are used to acquire time-varying surface static pressure data variations, which are synchronized with the high-speed shadowgraph flow visualization imaging sequences. These pressure transducers use silicon diaphragms with a fully active four-arm Wheatstone bridge to sense fluctuations in pressure and process the associated electronic signals. Each one of these devices includes an in-line auxiliary KEA-B-1B amplifier, each of which magnifies the output voltage from the Wheatstone bridge circuit inside the transducer. A Kulite B-screen is installed above each sensor location to protect each pressure diaphragm. For the present model, the natural frequency of each sensor is between 300 and 380 kHz. The installation locations of the Kulite pressure transducers (K1, K2, and K3) are shown in Fig. 3.

2.3 Shadowgraph flow visualization apparatus

Time-varying, shock wave structural characteristics are visualized using a shadowgraph system, which is described by Ligrani and Marko [10] and Manneschmidt and Ligrani [11]. Instantaneous images are captured from this system using an AF Micro-NIKKOR 200 mm 1:4D ED camera lens and a Phantom v711 high-speed camera (manufactured by the Ametek Materials Analysis Division of Vision Research Company).

3 Data acquisition and analysis procedures

3.1 Flow visualization data

The digitized flow visualization images from the Phantom V711 camera are acquired by the Phantom Camera Control PCC 2.7 software, as the associated ready signal is acquired using a National Instruments USB-6341 data acquisition card. This card is employed to synchronize the acquisition of the flow visualization images with the data acquired by the Kulite pressure transducers. Once the USB-6341 detects the ready signal, the USB-6341 notifies the LabVIEW 2020 version 20.0.1 software to start acquiring data for the Kulite pressure transducers through the cDAQ-9178 chassis. The ready signal is detected by LabVIEW once the user starts acquiring data in the Phantom Camera Control Application software. When employed in this manner, the data acquisition frequency is 10 kHz and is identical for each of the Kulite pressure transducers and the acquisition of the Phantom acquired digital camera images. Additional data analysis and processing are accomplished using MATLAB version R2019b software. With the present approach, the spatial resolution of each flow visualization image is 20 micrometers per pixel location. The exposure time is 1.0 μs for the sampling rate employed within the present investigation.

3.2 Surface static pressure data

Analog signals from the Kulite XCQ-062-5BarA pressure transducers are acquired using an NI 9239 data acquisition card. The NI 9239 data acquisition card is a National Instruments Voltage Input C Series Module, which has the capability of acquiring four different sensors up to 50 kHz and measures the amplified voltage provided by the KEA-B-1B in-line amplifier. The digital signals, which are provided by the NI 9238 data acquisition card and the cDAQ-9178 chassis, are acquired and recorded using LabVIEW 2020 version 20.0.1 software. The data acquisition frequency employed to acquire Kulite transducer pressure data is 10 kHz, as mentioned.

3.3 Shock wave position tracking

Shock wave instantaneous locations are tracked along horizontal lines that cross the shock wave using MATLAB version R2019b software. Such line flow placement locations are labelled A, E, and G, and are shown in Fig. 4a, b for high and low inlet unsteady Mach wave intensity, respectively. Each of these figure parts presents an instantaneous shadowgraph image for one individual digital frame showing different flow phenomena within the test section. Note that each of these line paths is located below the shock wave holding plate. Also note that, as part of this process, Microsoft Paint version 22H2 software is employed to determine the pixel location range in which the shock wave is expected.

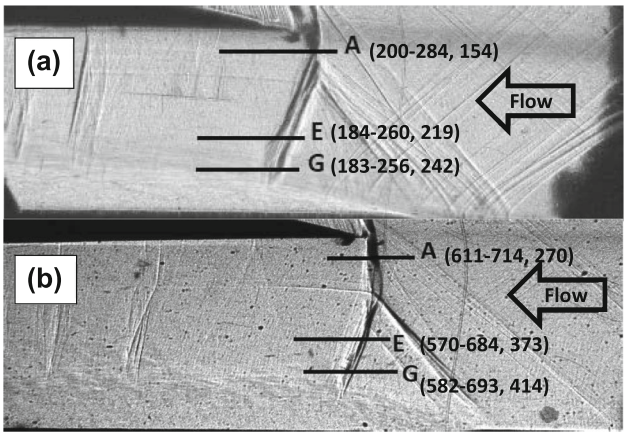

Fig. 4 Flow locations for tracking of shock wave time-varying positions. **a** High inlet unsteady Mach wave intensity. **b** Low inlet unsteady Mach wave intensity. Numbers in parentheses are pixel locations

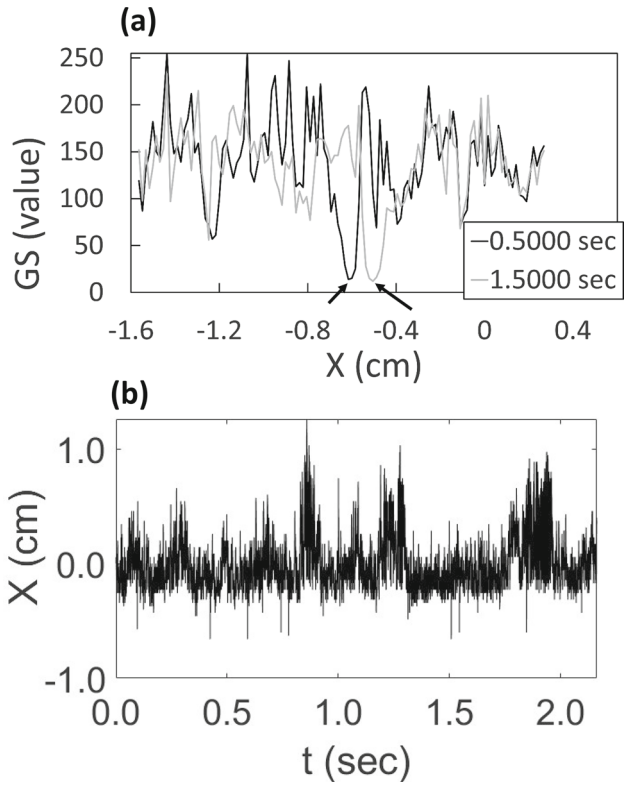

Fig. 5 Examples of results for determination of time-varying tracked locations of the normal shock wave with high inlet unsteady Mach wave intensity. **a** Local gray scale variations with streamwise location for two time values after initiation of data acquisition. **b** Time-varying tracked location of the normal shock wave

Examples of results for determination of time-varying tracked locations of the normal shock wave with high inlet unsteady Mach wave intensity, determined using these procedures, are shown in Fig. 5. To determine such data, pixel

intensity gray scale value variations with streamwise pixel location across the normal shock wave are first determined. The position of the normal shock wave along the line is then identified at the pixel value with the lowest gray scale value. This position is denoted with arrows in Fig. 5a. This method is appropriate since shock waves produce extreme local density changes and because shadowgraph visualizations show changes resulting from variations of the second derivative of the fluid density. Dimensional streamwise location variations are subsequently calculated by applying an appropriate scale conversion factor to time-varying pixel location values. Final data sequences employed for coherence and spectral analysis are then provided in fluctuation form, relative to time-averaged values, by subtracting time-averaged values from instantaneous signal values. An example of a time-varying tracked location of the normal shock wave, determined with this approach and employed for these purposes, is shown in Fig. 5b.

Additional details of associated analysis procedures are provided by Manneschmidt and Ligrani [11].

3.4 Power spectral density

Procedures to determine power spectral density information are described by Ligrani and Marko [10] and Manneschmidt and Ligrani [11]. Employed as part of this process as Welch's method is applied to time-varying data using MATLAB version R2019b software are a fifth-order Butterworth filter, and a 50% overlapping Hanning data window.

3.5 Magnitude-squared coherence and time lag

To determine magnitude-squared coherence and time lag data, the first step also involves the application of a fifth-order Butterworth filter by means of MATLAB version R2019b software to attenuate all frequencies above 90% of the Nyquist folding frequency. The analysis to determine magnitude-squared coherence variation with frequency is subsequently performed using the mscohere function, and time lag results as they vary with frequency are obtained using cross-power spectral density analysis with the cpsd function, where both of these functions are implemented using MATLAB software.

Resulting magnitude-squared coherence data provide information of flow phenomena which are interacting with each other in a coherent manner at different frequencies. Determined is C_{xy} to quantify the correlation between two datasets, as this parameter ranges from 0 to 1. Here C_{xy} is defined as the magnitude-squared coherence of signals x and y, where signals x and y are associated with different flow locations. Resulting C_{xy} data are occasionally very noisy, with greater data scatter as the frequency gets higher. A moving average is utilized to remedy this issue, wherein the number of points averaged varies with frequency within the smoothing algorithm.

After determination of cross-power spectral density results, the angle function within MATLAB software is used to convert the cross-power spectral density signal into a phase signal in radians. The resulting data represent the phase shift variation with frequency between the two original signals from two different flow locations. With the phase shift variation in hand, the unwrap function within MATLAB software is utilized. This function detects abrupt changes caused by phase shifts which are greater than π, and then makes appropriate corrections to the data. Resulting corrected phase shift data are then converted to time lag values in seconds, by considering the time period for each frequency. When spatially-varying time lag variations are determined, an additional unwrapping algorithm is applied to the data prior to the conversion of phase shift values to time lag magnitudes. This algorithm is provided by Kasim [12] and is based upon the work of Arevalillo-Herraez et al. [13]. Associated corrections within the algorithm are based upon spatial variations of phase shift magnitudes.

4 Experimental results and discussion

Provided within the present section are experimental results, and analysis of these results. Included are distributions of power spectral density, magnitude-squared coherence, and time lag data. Of particular focus are interactive relationships between the normal shock wave and the downstream shock wave leg of the lambda foot, as well as interactive relationships between the normal shock wave and time-varying static pressure as measured along the bottom surface of the test section. Such relationships are considered as they vary with two different magnitudes of inlet unsteady Mach wave intensity.

4.1 Test section inlet unsteady Mach wave intensity and magnitude-squared coherence relative to the normal shock wave

To quantify relative magnitudes of inlet unsteady Mach wave intensity, values of $\overline{P'^2}$ are determined for test section inlet locations, where P' is the instantaneous gray scale value for selected digitized video pixel locations. The process to determine $\overline{P'^2}$ is given by:

$$\overline{P'^2} = \frac{1}{N}\sum_{i=1}^{N}\left(P_i - \bar{P}\right)^2, \tag{1}$$

where P_i is the instantaneous gray scale value of a pixel for a single frame, $\bar{P}$ is the average value for multiple frames, and N is the number of frames.

This determination is undertaken over a region which is comprised of a total of nine adjacent image pixel frames. The inlet locations used to characterize and quantify augmented magnitudes of inlet unsteady Mach wave intensity are shown in Fig. 3 and are associated with the highest local density of unsteady Mach waves near the inlet of the test section. When such flow locations are considered, nine adjacent image pixel frames are used for determination of $\overline{P'^2}$ values because the use of a larger number of adjacent pixel frames gives approximately the same value of $\overline{P'^2}$. Because of varying camera exposure and lighting intensity settings for different sets of digital video sequence data, intensity values for characteristic inlet unsteady Mach wave regions are determined relative to regions of the flow which are relatively calm (without locally augmented Mach wave unsteadiness). Resulting data indicate that the overall inlet intensity for the flow arrangement with high inlet Mach wave unsteadiness is 2.76 times greater than the inlet intensity for the flow arrangement associated with low inlet Mach wave unsteadiness.

Note that flow freestream turbulence intensity is ordinarily defined as the time-averaged root-mean-square of fluctuating streamwise velocity divided by the local freestream streamwise velocity. Here, within the present investigation, inlet main flow unsteady Mach wave intensity is quantified as the mean-square magnitude of instantaneous gray scale value or $\overline{P'^2}$ (which is approximately time-averaged), normalized by the magnitude of $\overline{P'^2}$ for a quiescent region within the same flow arrangement. The result of this determination is employed both as the numerator and the denominator within a ratio which quantifies intensity associated with a flow arrangement having high inlet unsteady Mach wave intensity, relative to intensity for a different flow arrangement having low inlet unsteady Mach wave intensity. Such an approach assumes that quiescent region $\overline{P'^2}$ values are about the same for the two different flow arrangements. With this approach, the ratio of overall flow intensity ratio for the flow arrangement with high inlet Mach wave unsteadiness, relative to the flow arrangement ratio associated with low inlet Mach wave unsteadiness, is equal to 2.76.

Additional insight into the effects of inlet intensity is provided by the data within Fig. 6. Shown are magnitude-squared coherence variations for location A along the normal shock wave relative to test section inlet locations. Results in Fig. 6a are provided for high inlet unsteady Mach wave intensity. Results in Fig. 6b are provided for low inlet unsteady Mach wave intensity. Multiple local peaks are evident within the distribution in part a for high inlet unsteady Mach wave intensity, with values as high as about 0.24. Such characteristics evidence significant coherence interactions between test section inlet Mach waves and the normal shock wave. Such behavior illustrates the pervasive influences of inlet unsteady Mach waves on local flow structure, especially in relation to the normal shock wave. Within Fig. 6b for lower inlet unsteady Mach wave intensity, fewer magnitude-squared coherence peaks are present, with lower maximum magnitudes. Such characteristics indicate less influence and lower dominance of inlet Mach waves on flow structure, as shown by coherent interactions with the normal shock wave which are quantitatively less, relative to Fig. 6a data (for high inlet unsteady Mach wave intensity).

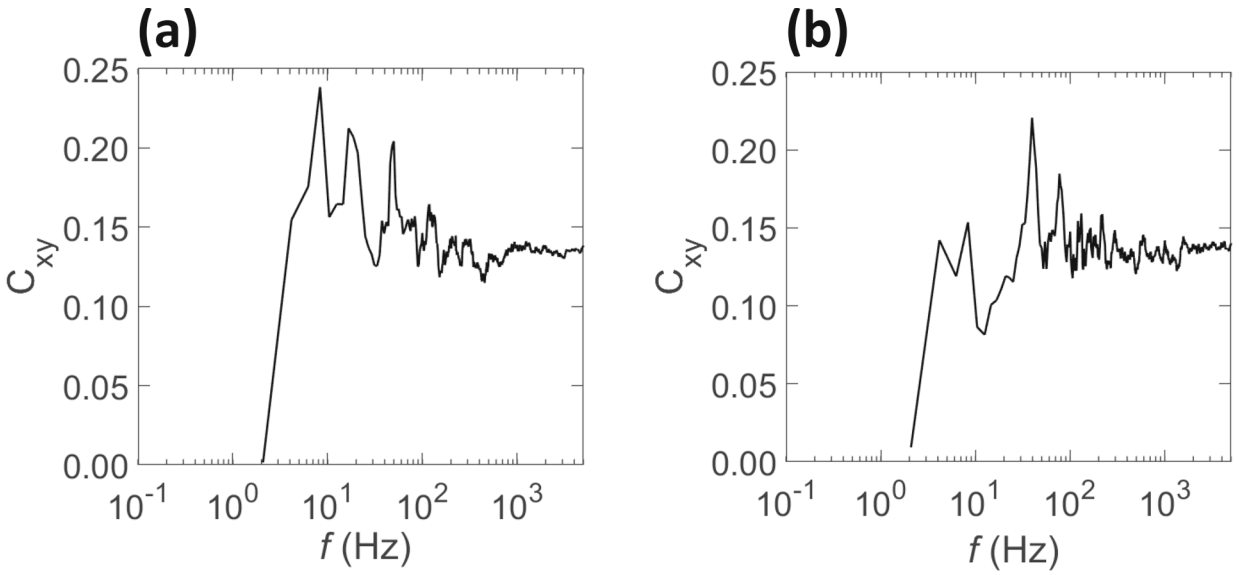

Fig. 6 Magnitude-squared coherence variation for location A along the normal shock wave relative to test section inlet locations. **a** High inlet unsteady Mach wave intensity. **b** Low inlet unsteady Mach wave intensity

4.2 Power spectral density variations of the normal shock wave and the downstream oblique shock wave leg of the lambda foot

Figure 7 shows comparisons of power spectral density distributions for high and low inlet unsteady Mach wave intensity. These data are provided for normal shock wave location A in Fig. 7a, for lambda foot downstream shock wave leg location E in Fig. 7b, and for lambda foot downstream shock wave leg location G in Fig. 7c.

Significant variations between these data sets are often present at frequencies less than around 200 Hz. For example, at these lower frequencies, spectral density magnitudes are often higher for high inlet unsteady Mach wave intensity for location G, when compared at the same frequency. In contrast, spectral density magnitudes are often higher for low inlet unsteady Mach wave intensity for locations A and E when compared at frequency values less than about 20 Hz. Notable differences between the high and low inlet unsteady Mach wave distributions are additionally apparent at a number of specific frequencies. For example, with 8 Hz, a local maximum peak is present for locations A, E, and G when inlet unsteady Mach wave intensity is low, and this local peak is not present with high inlet unsteady Mach wave intensity. Another example is a substantial dip at around 12 Hz with low inlet unsteady Mach wave intensity, which is not present within high inlet Mach wave unsteadiness data. Such differences are related to shock wave coherence, which is well defined with low inlet unsteady Mach wave intensity, but disrupted by unsteady test section inlet Mach waves with high inlet unsteady Mach wave intensity.

Power spectral density distributions for shock wave locations A, E, and G are compared within Fig. 8. These data are shown for high inlet unsteady Mach wave intensity in Fig. 8a, and for low inlet unsteady Mach wave intensity in Fig. 8b. Spectral distributions for high inlet unsteady Mach wave intensity are generally in quantitative agreement for all three shock wave locations at frequencies greater than about 150 Hz. At lower frequencies, the spectral distribution for location G is generally higher than distributions for locations A and E, when compared at the same frequency. With low inlet unsteady Mach wave intensity, distributions in Fig. 8b for all three shock wave locations are similar at frequencies greater than 100 Hz. At lower frequencies, the highest spectral density magnitudes are associated with locations A and E, and the lowest magnitudes are generally associated with location G. Another notable feature of the data in Fig. 8a, b is quantitative similarity of spectral distributions for locations A and E for both high and low inlet unsteady Mach wave intensity values.

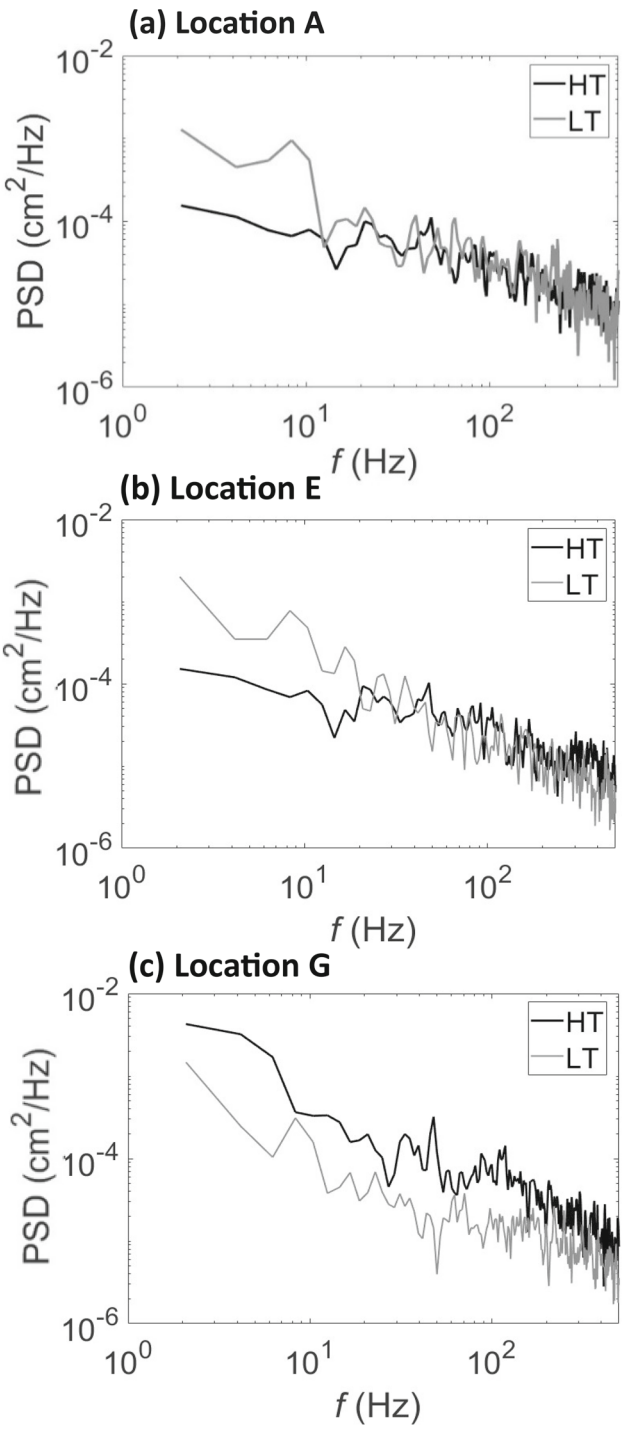

Fig. 7 Comparisons of power spectral density distributions for high and low inlet unsteady Mach wave intensity. **a** Normal shock wave location A. **b** Lambda foot downstream shock wave leg location E. **c** Lambda foot downstream shock wave leg location G

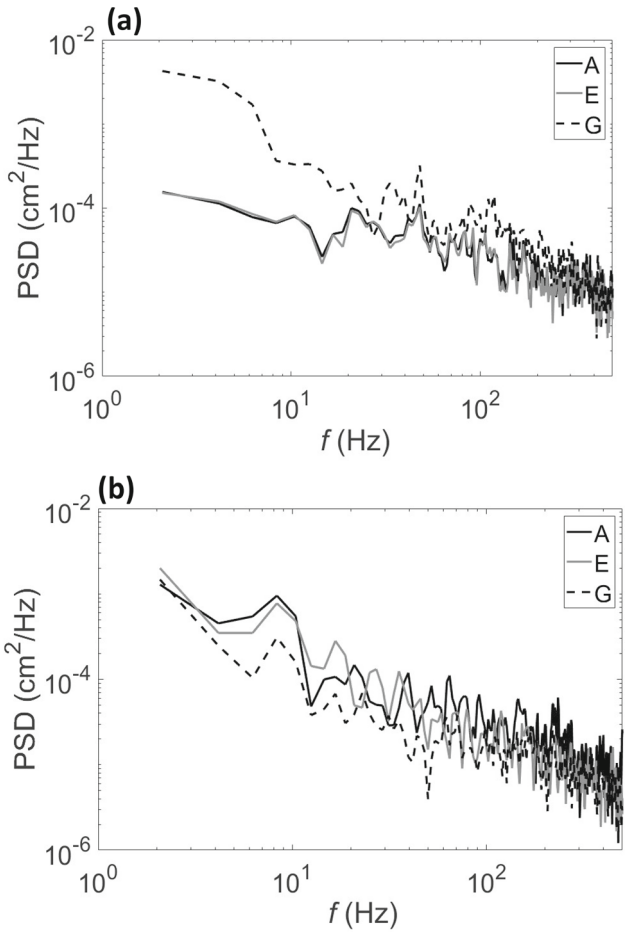

Fig. 8 Comparisons of power spectral density distributions for shock wave locations A, E, and G. **a** High inlet unsteady Mach wave intensity. **b** Low inlet unsteady Mach wave intensity

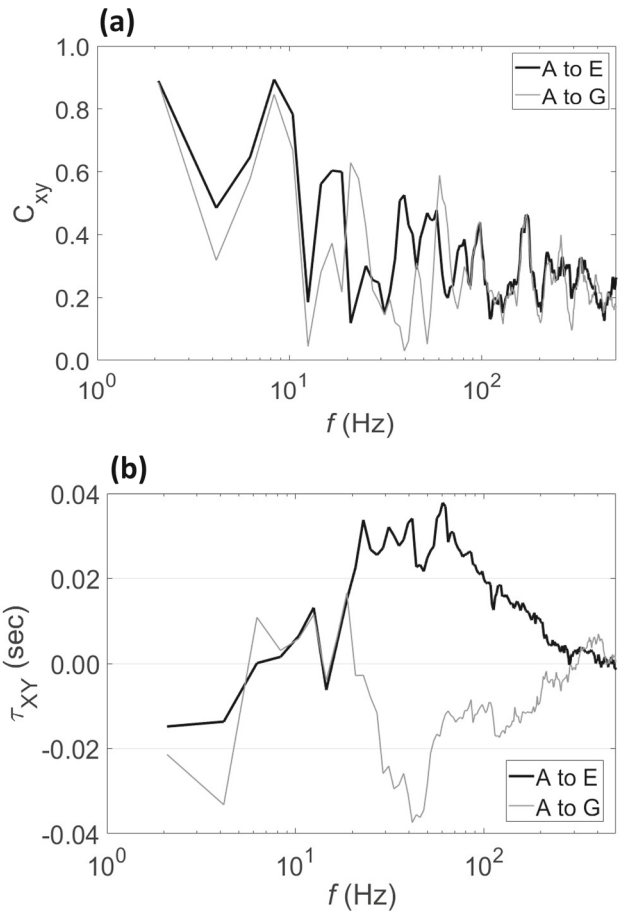

Fig. 9 Correlation quantities for normal shock wave location A relative to location E, and for normal shock wave location A relative to location G, as they vary with frequency for low inlet unsteady Mach wave intensity. **a** Magnitude-squared coherence. **b** Time lag, where negative values indicate that normal shock wave location A events occur prior to events at locations E and G

4.3 Magnitude-squared coherence and time lag of the normal shock wave relative to the downstream oblique shock wave leg of the lambda foot for low inlet unsteady Mach wave intensity

Figure 9 shows correlation quantities for normal shock wave location A relative to location E, and for normal shock wave location A relative to location G. These results are given as they vary with frequency for low inlet unsteady Mach wave intensity. Magnitude-squared coherence data are presented in Fig. 9a, and time lag data are presented in Fig. 9b. In regard to time lag variations, negative values indicate that normal shock wave location A events occur prior to events at locations E and G. Here, upper and lower refer to locations farther and closer to the bottom wall of the test section, respectively. According to Fig. 4, location A is positioned near the upper portion of the normal shock wave, whereas locations E and G are, respectively, positioned at upper and lower locations along the rearward shock wave leg of the lambda foot.

Figure 9a shows that the magnitude-squared coherence between location A relative to locations E and G on the rear lambda shock wave leg are quantitatively and qualitatively similar for the entire frequency range analyzed. Local maxima apparent within this figure are present for frequencies in the vicinity of 2 Hz, 8 Hz, 15 Hz, 23 Hz, 40 Hz, 60 Hz, 95 Hz, and 160 Hz. Here, coherence values are also sometimes higher than 0.8 for frequencies less than 10 Hz which indicates strong interactions with the normal shock wave.

The dominating influences of the normal shock wave for these frequencies are also illustrated by the time lag data in Fig. 9b. Here, negative values for frequencies less than 10 Hz mean that events occur first at normal shock wave location A, which is also the originating location of associated flow unsteadiness. Another interesting feature of Fig. 9b data is the similarity of time lag variations at frequencies between 10 and 20 Hz for the A–E and A–G data sets. Significant time lag differences between these data sets are then present

at higher frequency values. Values associated with A to E are then positive for frequencies up to about 1000 Hz, indicating that E location unsteady events occur prior to A location unsteady events. In contrast, values associated with A–G are negative for frequencies from 20 Hz to around 300 Hz, which shows that normal shock wave A location unsteady events occur prior to lambda foot oblique shock wave location G events. As such, evidence is provided of important interactions between the normal shock wave and the portion of the downstream lambda foot structure which is nearest to the flow separation zone beneath the lambda foot.

4.4 Magnitude-squared coherence and time lag of the normal shock wave relative to the downstream oblique shock wave leg of the lambda foot for high inlet unsteady Mach wave intensity

Figure 10 shows correlation quantities for normal shock wave location A relative to location E, and for normal shock wave location A relative to location G. These results are given as they vary with frequency for high inlet unsteady Mach wave intensity. Magnitude-squared coherence data are presented in Fig. 10a, and time lag data are presented in Fig. 10b. In regard to time lag variations, negative values indicate that normal shock wave location A events occur prior to events at locations E and G.

Figure 10a shows that, with high inlet Mach wave unsteadiness, the correlation between the upper portion of the normal shock wave associated with location A and the rearward shock wave leg of the lambda foot is generally strongest with respect to location G, near the lower portion of the shock wave leg. The highest magnitude-squared coherence values over the frequency range from 0 to 300 Hz are associated with location A as it is correlated relative to location G. This is also apparent as the correlation values for A to E are often significantly lower than A–G, when compared at particular values of frequency, especially for frequencies less than about 300 Hz. Here, C_{xy} values relative to location E generally range from 0.0 to 0.4, whereas values relative to location G range from 0.05 to 0.95. The trend of C_{xy} relative to location G is relatively high values at low frequencies, with generally decreasing values as frequency increases.

Figure 10b shows time lag values which deviate from zero for frequencies less than about 20 Hz for unsteady events correlated relative to locations E and G. Here, values are negative which means that location A normal shock wave events occur prior to events at the other locations. Values associated with location E are as low as about -0.02, whereas values associated with location G are lower than -0.04. For frequencies from 25 to 300 Hz, near zero time lag values indicate that flow events at locations associated with the rear lambda leg are generally moving without any delay relative to the normal shock wave.

Significant local maxima in magnitude-squared coherence distributions are evident within Fig. 10a at frequencies from 4 to 8 Hz, approximately 13 Hz, approximately 20 Hz, from 40 to 50 Hz, and from 80 to 130 Hz. These variations are present for both correlation pairs, A –E and A–G. Negative time lags are associated with the two lower frequency values, whereas near zero time lag values are associated with all the higher frequency values and frequency ranges.

The data in Figs. 9a, b and 10a, b show distinct interactions over a wider range of frequencies between the normal shock wave and the downstream shock wave leg of the lambda foot for low inlet unsteady Mach wave intensity. Note that these are not present in the same form and over the same

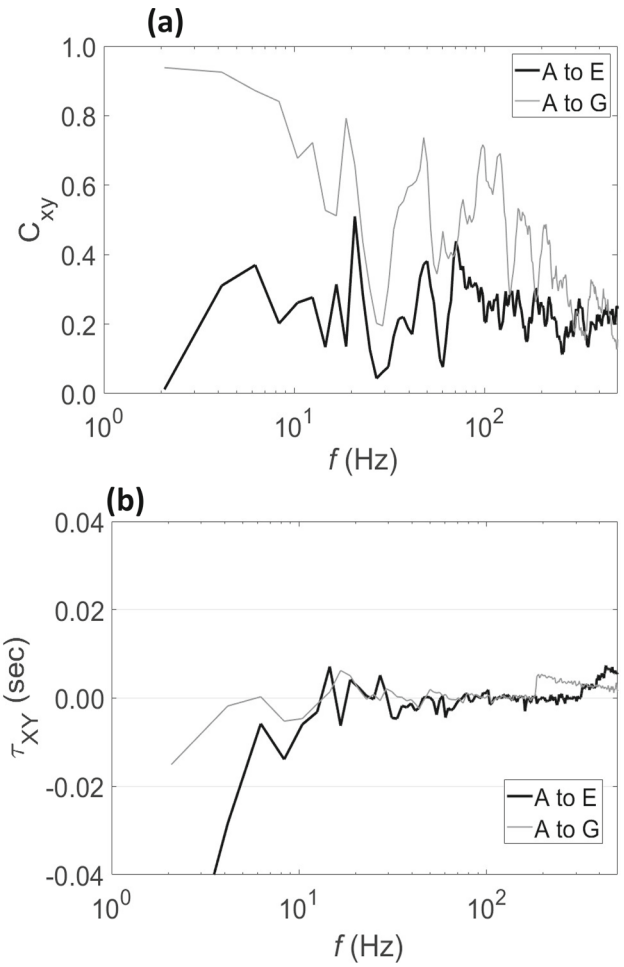

Fig. 10 Correlation quantities for normal shock wave location A relative to location E, and for normal shock wave location A relative to location G, as they vary with frequency for high inlet unsteady Mach wave intensity. **a** Magnitude-squared coherence. **b** Time lag, where negative values indicate that normal shock wave location A events occur prior to events at locations E and G

ranges of frequency with high inlet unsteady Mach wave intensity. These differences are partially due to the location where flow events originate. Note that all flow locations examined can be the originating source of flow unsteadiness, but the most significant sources within the present investigation are associated with the normal and oblique shock waves (with low inlet unsteady Mach wave intensity), and with inlet flow disturbances from unsteady Mach waves (with high inlet unsteady Mach wave intensity). If the causes of flow unsteadiness originate in the normal shock wave, they would then travel up or down the shock wave structure to propagate to the other locations, resulting in time lag variations like the ones shown in Fig. 9b for low inlet unsteady Mach wave intensity. With high inlet unsteady Mach wave intensity, if similar events are occurring, they appear to be overpowered and overwhelmed by the unsteadiness associated with the test section inlet Mach waves. The associated unsteady flow events would then affect large portions of the flow at a similar time (with near zero time lag values like the ones shown in Fig. 10b), including the inlet boundary layer, the lambda foot shock wave structures, the flow separation zone, and the normal shock wave, thus resulting in time lag values near zero.

Overall, the characteristics illustrated by the results in Fig. 10a and b additionally evidence important connections between the normal shock wave and unsteady flow events within lower portions of the lambda foot (rather than within the upper portions of the lambda foot), especially near the adjacent boundary layer separation region. This characteristic is also associated with high test section inlet unsteady Mach wave intensity from collections of unsteady and intersecting Mach waves. The influences of these oscillating waves appear to be spread across the entire inlet of the section as the flow approaches the leading edge of the shock wave holding plate. Significant disturbances then seem to be imposed throughout the flow on many subsequently developing events. As such, disturbances from upstream unsteady Mach waves then appear to be propagating through the boundary layer and into the separated boundary layer (near the lower portion of the lambda leg) around the same time they also affect the normal shock wave. As such, the highly unsteady Mach waves at the inlet are believed to be disturbing the flow much more strongly, relative to disturbances that originate in the normal shock wave. Images within Fig. 4a, b also suggest that the high inlet Mach wave unsteadiness also has a significant effect on boundary layer development upstream of the lambda foot.

Important connections between low-frequency shock wave unsteadiness and pulsations of the associated separation bubble are also illustrated by results which are presented by Dussauge et al. [14], Piponniau et al. [5], Pirozzoli et al. [8], Clemens and Narayanaswamy [9], and Grilli et al. [6]. Results from Grilli et al. [6] in particular, which also include unsteady surface pressure data, show coupling between motion of the recirculation region and the motion of the shock wave. Dussauge et al. [14] additionally suggest that the three-dimensional structure of the separation bubble may be the origin of shock wave unsteadiness. Priebe and Martin [15] indicate that the physical origin of the shock wave low-frequency unsteadiness is breathing of the separation bubble and flapping of the separated shear layer, especially as these phenomena are tied to the inherent instability in the downstream separated flow. Several of these sources also indicate that the characteristic low frequency of motion associated with the foot of a normal shock wave is significantly lower, by as much as three orders of magnitude, relative to characteristic frequency of the oncoming boundary layer [6, 8, 14, 16]. Many of these observations are in agreement with experimental results from Piponniau et al. [5], as well as with results from the present investigation, especially in regard to interactions between the normal shock wave and the separation/recirculation flow region beneath the lambda foot, as well as in regard to the associated unsteady phenomena frequency magnitudes.

4.5 Magnitude-squared coherence and time lag of the normal shock wave relative to surface static pressure

Figure 11 presents correlation quantities for normal shock wave location A relative to Kulite transducer time-wise pressure variations as they vary with frequency. These data are provided for high inlet unsteady Mach wave intensity. Figure 11a shows magnitude-squared coherence data, and Fig. 11b shows time lag data, where negative values indicate that normal shock wave location A events occur prior to events at Kulite pressure transducer measurement locations shown in Fig. 3.

Overall, results within Fig. 11 illustrate important influences and effects of the normal shock wave. This is indicated in Fig. 11b by events which originate and occur first at the normal shock wave location, especially for frequencies less than around 10 Hz. Near zero time lag values for higher frequencies are connected to the influences of high inlet unsteady Mach wave intensity, especially as a result of a myriad of unsteady oblique Mach waves, which are present over most of the spatial area of the test section inlet region.

Magnitude-squared coherence data within Fig. 11a also evidence important interactions between normal shock wave unsteadiness and unsteady static pressure measured along the test section bottom surface. Of particular note are more pronounced coherence magnitudes of the normal shock wave relative to the downstream boundary layer at the K3 transducer location and beneath the lambda foot at the K2 transducer location. Magnitude-squared coherence values relative to the upstream boundary layer, in regard to the

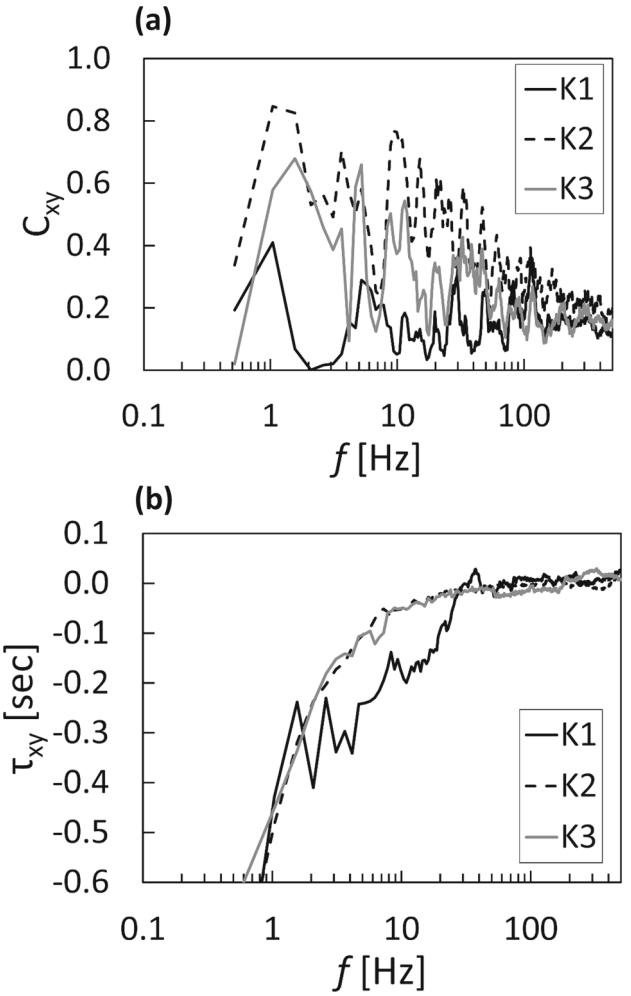

Fig. 11 Correlation quantities for normal shock wave location A relative to Kulite transducer time-wise pressure variations as they vary with frequency for high inlet unsteady Mach wave intensity. **a** Magnitude-squared coherence. **b** Time lag, where negative values indicate that normal shock wave location A events occur prior to events at Kulite transducer locations

K1 location, are significantly less, when compared at particular frequency values. However, even though coherence magnitudes associated with different transducer locations vary, local maximum events occurring at specific frequency values are often present at the same frequency values for all three Kulite locations K1, K2, and K3. These are especially evident for frequencies in the vicinity of 1 Hz, 8 Hz, 10–15 Hz, and for additional specific frequency values between 15 and 100 Hz.

Highly correlated interactions between shock waves, associated flow separation zones, and downstream boundary layers are also reported by Wu and Martin [7], Priebe and Martin [15], Piponniau et al. [5], and Grilli et al. [6]. According to these investigators, upstream boundary layer unsteadiness is not responsible for shock wave interaction unsteadiness.

4.6 Magnitude-squared coherence and time lag comparisons for high and low inlet unsteady Mach wave intensity

Figures 12 and 13 present comparisons of magnitude-squared coherence and time lag, respectively, for high and low inlet unsteady Mach wave intensity. In both cases, data variations with frequency are provided. Data within a parts of these figures are determined for normal shock wave location A relative to location E, and data within b parts of these figures are determined for normal shock wave location A relative to location G. The data within Figs. 12a and 13a provide information on interactions between the normal shock wave (location A) and the upper portion of the downstream oblique shock wave associated with the lambda foot (location E). Figure 12a shows relatively high values of magnitude-squared coherence at multiple frequency values for low inlet unsteady Mach wave intensity (LT). These are generally significantly larger than values for high inlet unsteady Mach wave intensity (HT), when compared at the same frequency. The only exceptions, with locally higher HT values, are evident only for frequencies of 16 Hz and around 65 Hz. Of particular interest is the prominent coherence peak at about 8 Hz for the low Mach wave unsteadiness case, whereas associated peaks at nearby frequency values for the high Mach wave unsteadiness case are less apparent. Overall, the data within Fig. 12a show that, even though amplitudes are different for events associated with local maximum values, coherence events often occur at the same frequency values for both inlet levels of Mach wave unsteadiness.

Time lag data provided within Fig. 13a provide additional perspectives on these comparisons and the associated flow interactions. For lower frequency values, time lag data for the two inlet intensity values show some consistency. Here, negative time lag values indicate that events occur first at normal shock wave location A, as effects then propagate to the oblique lambda foot leg at location E. For high inlet unsteady Mach wave intensity, this propagation arrangement is present for frequencies up to about 10 Hz. For low inlet unsteady Mach wave intensity, this propagation arrangement is present for frequencies up to about 6 Hz. When frequencies are higher and inlet unsteady Mach wave intensity is high, time lag values are consistently near zero which evidences simultaneous events at locations A and E. However, when frequencies are higher than 6 Hz and inlet unsteady Mach wave intensity is low, time lag values are often substantial, such that events associated with the lambda foot shock wave occur prior to normal shock wave events. This behavior is present for frequencies up to about 200 Hz, where time lag values are then near zero for higher frequencies, provided inlet unsteady Mach wave intensity is low.

Overall comparisons of data in Figs. 12a and 13a, with results in Figs. 12b and 13b, show dramatically different cor-

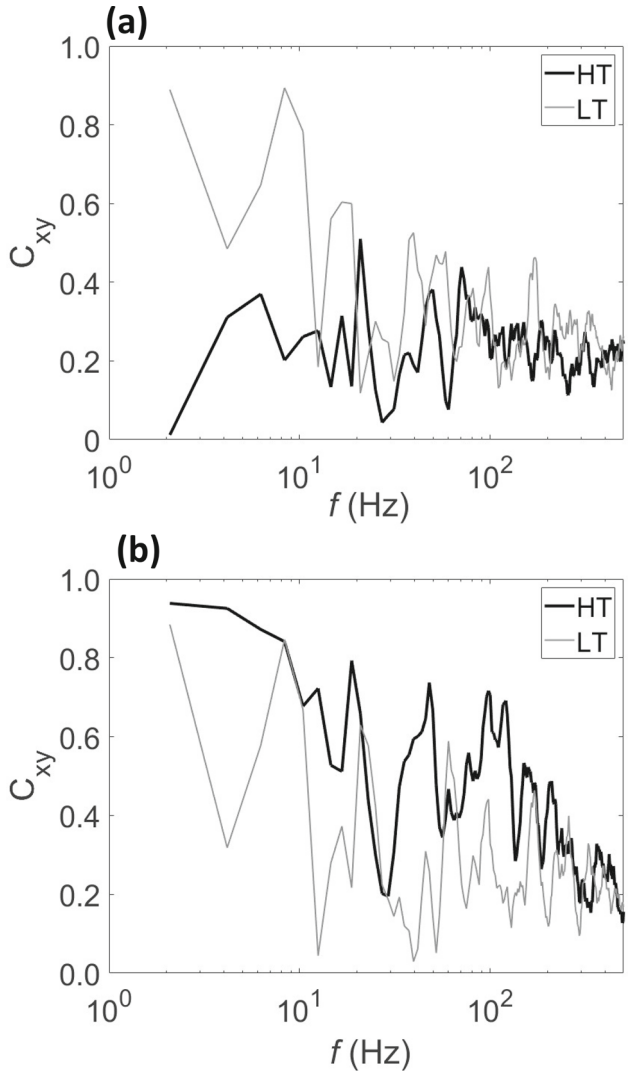

Fig. 12 Comparisons of magnitude-squared coherence variation with frequency for high and low inlet unsteady Mach wave intensity. **a** Normal shock wave location A relative to location E. **b** Normal shock wave location A relative to location G

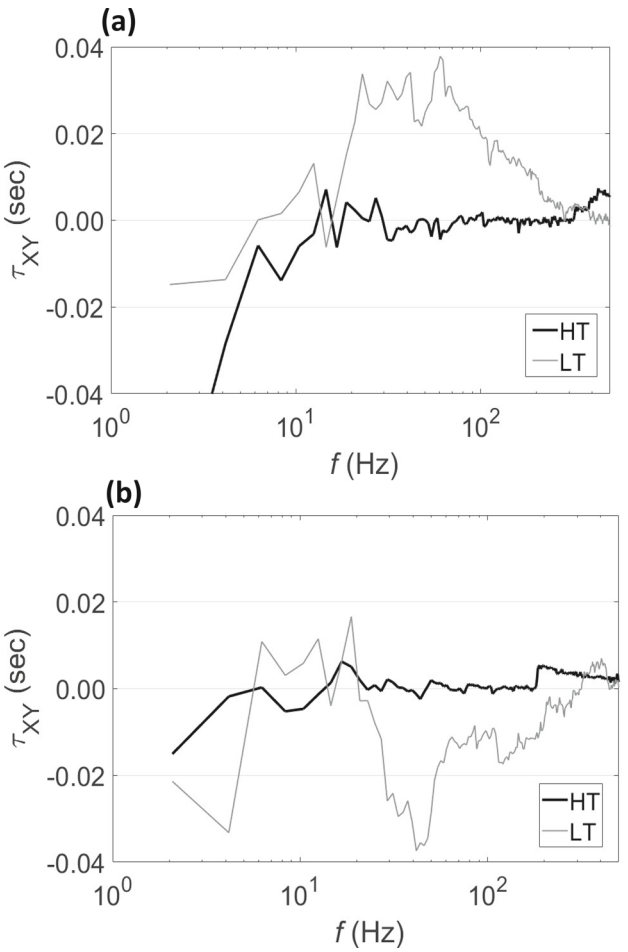

Fig. 13 Comparisons of time lag variation with frequency for high and low inlet unsteady Mach wave intensity, where negative time lag values indicate that normal shock wave location A events occur prior to events at locations E and G. **a** Normal shock wave location A relative to location E. **b** Normal shock wave location A relative to location G

relation behavior. This means that interactions of the normal shock wave with the upper and lower portions of the lambda foot shock wave are different. Such variations are believed to be present because the lower portion of the lambda foot shock wave is somewhat tied and controlled to unsteadiness associated with the flow recirculation and separation zone. This zone is of course located immediately below the lambda foot where flow is locally subsonic. Another interesting characteristic is stronger correlation of events connected to normal shock wave location A with events at lower lambda foot wave at G, compared to events at upper lambda foot wave at E. Such an observation evidences important interactions and connections between the normal shock wave and the flow recirculation-separation region. The data within Figs. 12b and 13b provide information on interactions between the normal shock wave (location A) and the lower portion of the downstream oblique shock wave associated with the lambda foot (location G). Here, as for results in the previous figure, data within Fig. 12b show that events associated with local maximum coherence values often occur at the same frequency values for both inlet unsteadiness levels. However, these data are different because distributions for high and low inlet unsteadiness are either of similar magnitude, or coherence values are locally larger for high inlet unsteady Mach wave intensity. Particularly noteworthy are local maxima in the vicinities of 8Hz, 10 Hz, 15–18 Hz, 40–50 Hz, 80–110 Hz, around 160 Hz, and around 200 Hz. Overall, such characteristics provide evidence of powerful and significant coherence and interactions between events at locations A and G, which are present regardless of the magnitude of inlet unsteady Mach wave intensity. As such, further illustration is provided of events and motions which are coherent and connected between the normal shock wave, the lower portions

of the oblique downstream shock wave associated with the lambda foot, and probably the flow recirculation-separation zone beneath the lambda foot.

Time lag data with high inlet unsteady Mach wave intensity for location A relative to location G in Fig. 13b are qualitatively similar to results in the previous figure. Negative values are present for frequencies up to about 10 Hz, with near zero values for most higher frequencies. The negative magnitudes at lower frequencies indicate that events associated with the normal shock wave at location A occur prior to oblique shock wave events at location G. Also of particular interest and significance are different time lag variations for low inlet unsteady Mach wave intensity in Fig. 13b for location A relative to location G, relative to time lag variations for low inlet unsteady Mach wave intensity in Fig. 13a for location A relative to location E. Within Fig. 13b, negative time lags are present for frequencies less than about 6 Hz and for frequencies between 15 and 300 Hz evidencing event origination at the normal shock wave. In contrast, positive lags between 6 and about 15 Hz provide a fascinating characteristic wherein event origination is associated with the G oblique shock wave location. Overall, with low inlet unsteady Mach wave intensity, events at the normal shock wave location A dominate flow behavior relative to oblique shock wave location G, with relatively high values of magnitude-squared coherence. Also present are event origination and unsteady events which occur first for many frequencies. With high inlet unsteady Mach wave intensity, normal shock wave events dominate events relative to oblique shock wave location G for lower frequencies less than 10 Hz, whereas inlet unsteady Mach wave intensity unsteadiness dominates events at most higher frequency ranges.

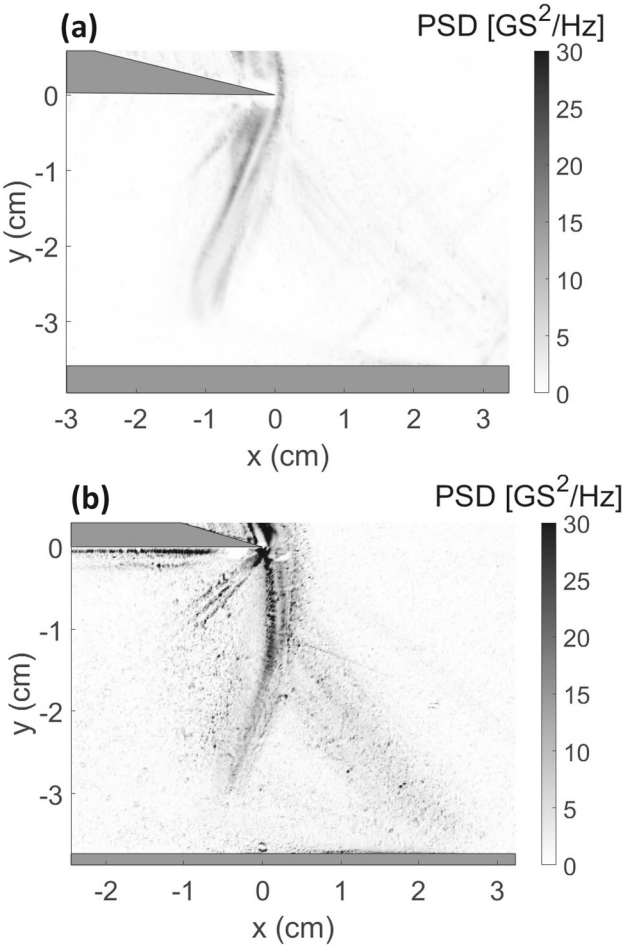

Fig. 14 Spatially-resolved power spectral density distributions for a frequency of 8.33 Hz. **a** High inlet unsteady Mach wave intensity. **b** Low inlet unsteady Mach wave intensity

4.7 Spatially-resolved power spectral density variations

Figure 14 presents spatially-resolved power spectral density distribution for a frequency of 8.33 Hz. Figure 14a gives data for high inlet unsteady Mach wave intensity, and Fig. 14b gives data for low inlet unsteady Mach wave intensity. These results are determined from local gray scale variations for each pixel of a time-varying video data sequence. The selection of 8.33 Hz for analysis is based upon data within Figs. 7 and 8, where important differences in unsteady flow structural characteristics are present between the high and low inlet unsteadiness configurations. In particular, the low inlet unsteady Mach wave intensity data show a distinct spectral peak in the vicinity of 8.33 Hz, whereas no similar local maximum value is present within the high inlet unsteady Mach wave intensity data.

Figure 14a, for high inlet unsteady Mach wave intensity, only shows the presence of significant spectral energy for flow locations associated with the normal shock wave and the downstream shock wave leg of the lambda foot. Note that power spectral density values associated with the forward shock wave leg of the lambda foot are very low in magnitude and spread out over a large area. Such characteristics are partially a consequence of locally intense flow disturbances and unsteadiness which are associated with high inlet unsteadiness. One consequence is that the upstream oblique shock wave is spread and positioned over a range of flow locations as time proceeds.

Locally augmented spectral energy values within Fig. 10b (for low inlet unsteady Mach wave intensity) are present at locations associated with the downstream oblique shock wave and the normal shock wave. Local signatures associated with the upstream oblique shock wave are also evident within this figure. However, local spectral energy augmentations are lower than for other flow locations and are spread over a relatively large flow area. Such upstream shock wave values are again partially a result of increased local unsteadi-

ness which spreads shock wave positions over a larger flow volume (relative to the other shock waves).

Note that the results within Fig. 14a, b provide evidence that the shock wave signatures, shown by locally augmented spectral variations, are associated with portions of the flow structure which are the most highly organized from temporal and spatial perspectives. Time-varying Mach waves, associated with high inlet unsteady Mach wave intensity and mostly located upstream of the shock wave structures, are then more random and disorganized types of flow events.

4.8 Spatially-resolved magnitude-squared coherence variations

Figure 15 shows spatially-resolved magnitude-squared coherence distributions for a frequency of 8.33 Hz for the normal shock wave dot location relative to other flow locations. Results in Fig. 15a are provided for high inlet unsteady Mach wave intensity, and results in Fig. 15b are provided for low inlet unsteady Mach wave intensity.

The data in both figure parts show high coherence values, relative to dot location unsteadiness, along normal shock wave locations, as well as along oblique shock wave locations on the upstream and downstream sides of the lambda foot. The low inlet unsteady Mach wave intensity data in Fig. 15b also show that relatively high magnitude-squared coherence values are only present for flow locations which follow the paths of the normal shock wave and the two oblique shock waves. Values are then consistently less than 0.2 for all other flow field locations, indicating very weak correlation.

The data in Fig. 15a for high inlet unsteady Mach wave intensity generally show larger variations of the flow locations which are associated with the normal and oblique shock waves. Another important feature of these data is evidence of significant correlations between the selected normal shock wave dot location and especially the upstream inlet area where flow is supersonic. However, also evident are significant correlations between the dot location relative to the area downstream of the shock waves, the upper part of the lambda foot separation zone, the subsonic flow separation zone, and subsonic downstream boundary layer. Overall, the spatial distribution of the magnitude-squared coherence indicates a chaotic and highly disturbed flow field. As such, additional illustration is provided of the spatial extent of disturbances from inlet unsteady Mach wave intensity, and the associated Mach waves, as they appear to affect most of the flow field, and associated flow events from the test section inlet to locations downstream of the normal and oblique shock waves.

4.9 Spatially-resolved time lag variations

Figure 16 presents spatially-resolved time lag variations for the high and low inlet unsteadiness cases at a frequency of

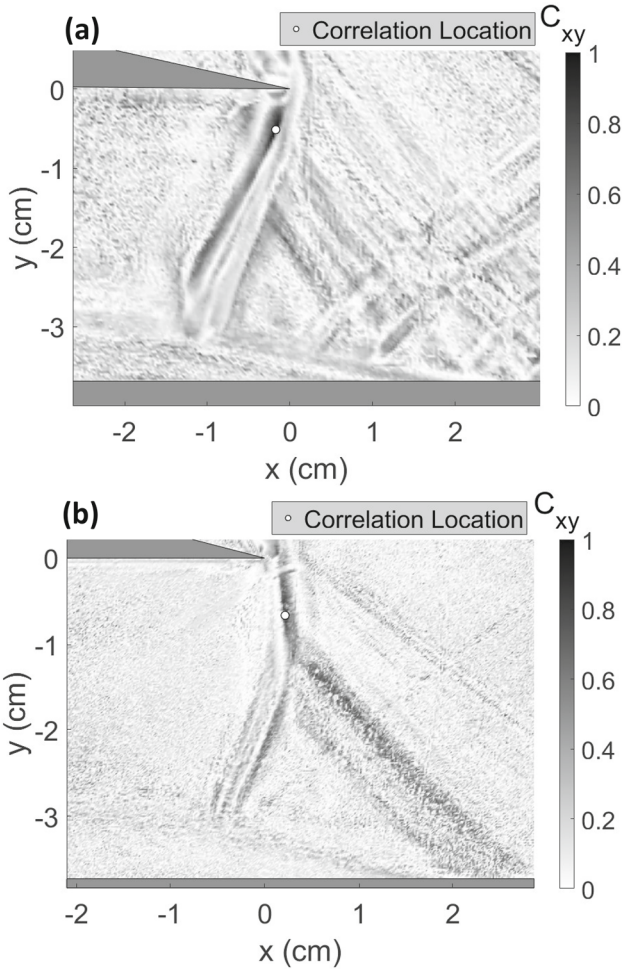

Fig. 15 Spatially-resolved magnitude-squared coherence distributions for a frequency of 8.33 Hz for normal shock wave dot location relative to other flow locations. **a** High inlet unsteady Mach wave intensity. **b** Low inlet unsteady Mach wave intensity

8.33 Hz. As mentioned, data at this frequency are selected for analysis because of important differences in unsteady flow structural characteristics for the high and low inlet unsteadiness configurations. For the data within Fig. 16, negative time lag values indicate that normal shock wave events which are present at the dot location occur prior to events and phenomena at other flow locations. Figure 16a displays results for high inlet unsteady Mach wave intensity, whereas Fig. 16b shows results for low inlet unsteady Mach wave intensity. The data within Fig. 16 are provided for the same locations and conditions as the spatially-resolved magnitude-squared coherence data in Fig. 15. Note that both sets of data within Fig. 16 have been spatially smoothed because of several small physically unrealistic local trends which are caused by phase unwrapping data corrections.

Results in Fig. 16a, b are consistent with data provided within Fig. 10a, b for high inlet unsteady Mach wave intensity. For a frequency of 8.33 Hz, results from both sources for

location A relative to locations E and G show very small time lag values, and significant correlation coefficients, especially when normal shock wave location A is considered relative to oblique lambda foot location G. When data relative to Kulite transducer location K2 are considered in regard to data within Fig. 11a, b, a similar conclusion is reached. Here, associated magnitude-squared coherence values are again relatively high and time lag values are also near to zero, which is consistent with spatially-resolved time lag distributions in Fig. 16a for high inlet unsteady Mach wave intensity.

Figure 16a, b also shows that the time lag values for the low inlet unsteady Mach wave intensity condition are generally much greater (in absolute value) than values associated with the high inlet unsteady Mach wave intensity arrangement, provided data are compared at similar flow locations. Within Fig. 16b, results provide evidence that the normal shock wave and forward lambda foot shock wave leg are moving in an approximately simultaneous mode. In contrast, the rearward lambda foot shock wave leg lags behind the normal shock wave by approximately 0.1 s. The shock waves appear to be the source of unsteadiness for flow events which are present immediately upstream and immediately downstream, as well as within the upper portions of the lambda foot. This is because the shock wave unsteadiness occurs prior to events at these other flow locations. In addition, results in Fig. 16b show that subsonic flow events within the separation region, located beneath the lambda foot, and within the downstream boundary layer, are occurring in advance of events which are associated with the normal shock wave.

In contrast, data within Fig. 16a show that, for the high inlet unsteady Mach wave intensity case, no significant values of time lag are present for any local flow location. Such an observation means that all events within the flow are simultaneous, which is a consequence of the dominating influences of augmented inlet unsteady Mach wave intensity. As a result, associated inlet flow unsteadiness affects all flow structural

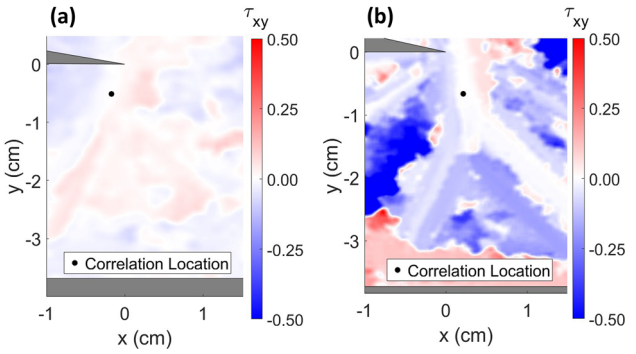

Fig. 16 Spatially-resolved time lag distributions for a frequency of 8.33 Hz, where negative time lag values indicate that normal shock wave events associated with the dot location occur prior to events at other flow locations. **a** High inlet unsteady Mach wave intensity. **b** Low inlet unsteady Mach wave intensity

characteristics, including the normal shock wave, the oblique shock waves associated with the lambda foot, the flow separation zone positioned beneath the lambda foot, and the upstream approaching boundary layer. Such characteristics illustrate increased correlation between different flow locations for the entire flow field when the inlet unsteady Mach wave intensity is high.

5 Summary and conclusions

A specialty test section is employed with an inlet Mach number of 1.54, as utilized within a transonic/supersonic wind tunnel, to investigate different inlet flow conditions as they affect shock wave structure and interactions. Of particular focus are interactive relationships between a normal shock wave and the downstream shock wave leg of the associated lambda foot, as well as interactive relationships between a normal shock wave and time-varying static pressure as measured along the bottom surface of the test section. Such relationships are considered as they vary with two different magnitudes of inlet unsteady Mach wave intensity (as quantified by low and high intensity levels) and are characterized using shadowgraph flow visualization data, as well as distributions of power spectral density, magnitude-squared coherence, and time lag data.

The resulting data provide evidence of distinct interactions over a wide range of frequencies between the normal shock wave and the downstream shock wave leg of the lambda foot for low inlet unsteady Mach wave intensity. Note that these are not present in the same form and over the same ranges of frequency with high inlet unsteady Mach wave intensity. These differences are partially due to the location where flow events originate. Note that all flow locations examined can be the originating source of flow unsteadiness, but the most significant sources within the present investigation are mostly associated with the normal and oblique shock waves (with low inlet unsteady Mach wave intensity), and mostly with inlet flow disturbances from unsteady Mach waves (with high inlet unsteady Mach wave intensity). When flow unsteadiness originates within the normal shock wave, they then travel along the shock wave structure to propagate to the other locations, resulting in time lag variations like the ones observed with low inlet unsteady Mach wave intensity. With high inlet unsteady Mach wave intensity, if similar events are occurring, they appear to be overpowered and overwhelmed by the unsteadiness associated with the test section inlet Mach waves, which is in the form of families of unsteady Mach waves. The associated unsteady flow events (with high inlet unsteady Mach wave intensity) then appear to affect large portions of the flow with near zero time lag values, including the inlet boundary layer, the lambda foot shock wave structures, the flow separation zone, and the normal shock

wave. In addition, the high inlet unsteady Mach wave intensity environment shows pronounced coherence magnitudes of the normal shock wave relative to Kulite pressure transducer locations beneath the downstream boundary layer and beneath the lambda foot. Magnitude-squared coherence values relative to static pressure variations beneath the upstream boundary layer are then significantly less, when compared at particular frequency values.

The present experimental results additionally evidence important connections between the normal shock wave and unsteady flow events within lower portions of the lambda foot (rather than within the upper portions of the lambda foot), especially near the adjacent boundary layer separation region. This characteristic is associated with low inlet unsteady Mach wave intensity and with high inlet unsteady Mach wave intensity. However, in spite of this commonality, the nature of the interactions between these different flow locations for the two inlet unsteady Mach wave intensity levels are significantly different. With low inlet unsteady Mach wave intensity, the dominating influences of the normal shock wave at frequencies less than 10 Hz are evidenced by time lag data, which show that events occur first at normal shock wave location A. This means that this location is also the originating location of associated flow unsteadiness. Additional time lag results show that, for frequencies from 20 Hz to values ranging from 300 to 1000 Hz, events associated with the upper portion of the oblique leg occur prior to normal shock wave events, whereas events associated with the lower portion of the oblique leg occur after normal shock wave events. As such, evidence is provided of important influences of the normal shock wave on the portion of the downstream lambda foot structure which is nearest to the flow separation zone beneath the lambda foot (provided the inlet unsteady Mach wave intensity is low).

For both levels of inlet unsteady Mach wave intensity, spatially-varying magnitude-squared coherence variations, for events occurring at a frequency of 8.33 Hz, show high coherence values, relative to specific normal shock wave location unsteadiness, along normal shock wave locations, as well as along oblique shock wave locations on the upstream and downstream sides of the lambda foot. The low inlet unsteady Mach wave intensity data show that such coherence values are only present for these flow locations. In contrast, coherence data with high inlet unsteady Mach wave intensity show significant correlations between the selected normal shock wave location and especially the upstream inlet area where flow is supersonic. Also present are significant correlations between the inlet flow and the normal shock wave relative to the area downstream of the shock waves, the upper part of the lambda foot separation zone, the subsonic flow separation zone, and subsonic downstream boundary layer. With high inlet unsteady Mach wave intensity, evidence is thus provided of a chaotic and highly disturbed flow field.

Associated spatially-resolved time lag data (also for events occurring at a frequency of 8.33 Hz) for low inlet unsteady Mach wave intensity provide evidence that the normal and oblique shock waves appear to be the source of unsteadiness for flow events which are present immediately upstream and immediately downstream, as well as within the upper portions of the lambda foot. Low inlet Mach wave unsteadiness data additionally show that subsonic flow events within the separation region, located beneath the lambda foot, and within the downstream boundary layer, are occurring in advance of events which are associated with the normal shock wave. In contrast, time lag data for the high inlet unsteady Mach wave intensity show no significant values are present for any local flow location. Such an observation means that all events within the flow are simultaneous, which is a consequence of the dominating influences of high inlet unsteady Mach wave intensity when it is present.

Acknowledgements The present research effort was funded by the CBET Thermal Transport Processes Program, National Science Foundation, Award Number 2041618. Ms. Sophie Nitschke is also acknowledged for her activities in obtaining preliminary results for the present investigation.

Declarations

Conflict of interest None of the authors have any financial or non-financial interests that are directly or indirectly related to the present work.

References

1. Humble, R.A., Elsinga, G.E., Scarano, F., van Oudheusden, B.W.: Three-dimensional instantaneous structure of a shock wave/turbulent boundary layer interaction. J. Fluid Mech. **622**, 33–62 (2009). https://doi.org/10.1017/S0022112008005090
2. Ganapathisubramani, B., Clemens, N.T.: Effects of upstream boundary layer on the unsteadiness of shock induced separation. J. Fluid Mech. **585**, 369–394 (2007). https://doi.org/10.1017/S0022112007006799
3. Ganapathisubramani, B., Clemens, N.T.: Low frequency dynamics of shock induced separation in a compression ramp interaction. J. Fluid Mech. **636**, 397–436 (2009). https://doi.org/10.1017/S0022112009007952
4. Touber, E., Sandham, N.D.: Low-order stochastic modelling of low frequency motions in reflected shock-wave/boundary-layer interactions. J. Fluid Mech. **671**, 417–465 (2011). https://doi.org/10.1017/S0022112010005811
5. Piponniau, S., Dussauge, J.P., Debieve, J.F., Dupont, P.: A simple model for low-frequency unsteadiness in shock-induced separation. J. Fluid Mech. **629**, 87–108 (2009). https://doi.org/10.1017/S0022112009006417
6. Grilli, M., Schmid, P.J., Hickel, S., Adams, N.A.: Analysis of unsteady behavior in shockwave turbulent boundary layer interaction. J. Fluid Mech. **700**, 16–28 (2012). https://doi.org/10.1017/jfm.2012.37
7. Wu, M., Martín, M.P.: Analysis of shock motion in shockwave and turbulent boundary layer interaction using direct numerical simulation data. J. Fluid Mech. **594**, 71–83 (2008). https://doi.org/10.1017/S0022112007009044

8. Pirozzoli, S., Larsson, J., Nichols, J.W., Bernardini, M., Mogan, B.E., Lele, S.K.: Analysis of unsteady effects in shock/boundary layer interactions. Annu. Res. Briefs **2010**, 153–164 (2010)
9. Clemens, N.T., Narayanaswamy, V.: Low-frequency unsteadiness of shock wave turbulent boundary layer interactions. Annu. Rev. Fluid Mech. **46**, 469–492 (2014). https://doi.org/10.1146/annurev-fluid-010313-141346
10. Ligrani, P.M., Marko, S.R.: Parametric study of wind tunnel test section configurations for stabilizing normal shock wave structure. Shock Waves **30**(1), 77–90 (2020). https://doi.org/10.1007/s00193-019-00911-5
11. Manneschmidt, W., Ligrani, P.M.: Statistical analysis of unsteady, spatially-varying shock wave characteristics within a supersonic flow environment. Int. J. Stat. Appl. **13**(1), 13–19 (2023). https://doi.org/10.5923/j.statistics.20231301.02
12. Kasim, M.F.: Fast 2D phase unwrapping implementation in MATLAB. https://github.com/mfkasim91/unwrap_phase (2017)
13. Arevalillo-Herraez, M., Burton, D.R., Lalor, M.J., Gdeisat, M.A.: Fast two-dimensional phase-unwrapping algorithm based on sorting by reliability following a non-continuous path. Appl. Opt. **41**(35), 7437–7444 (2002). https://doi.org/10.1364/AO.41.007437
14. Dussauge, J.-P., Dupont, P., Debieve, J.-F.: Unsteadiness in shock wave boundary-layer interactions with separation. Aerosp. Sci. Technol. **10**, 85–91 (2006). https://doi.org/10.1016/j.ast.2005.09.006
15. Priebe, S., Martín, M.: Low-frequency unsteadiness in shock wave-turbulent boundary layer interaction. J. Fluid Mech. **699**, 1–49 (2012). https://doi.org/10.1017/jfm.2011.560
16. Dolling, D.S., Murphy, M.T.: Unsteadiness of the separation shock wave structure in a supersonic compression ramp flow field. AIAA J. **21**, 1628–1634 (1983). https://doi.org/10.2514/3.60163